

# Large Damping Enhancement in Dirac-Semimetal–Ferromagnetic-Metal Layered Structures Caused by Topological Surface States

Jinjun Ding, Chuanpu Liu, Yuejie Zhang, Vijaysankar Kalappattil, Rui Yu, Uppalaiah Erugu, Jinke Tang, Haifeng Ding, Hua Chen, and Mingzhong Wu\*

This article reports damping enhancement in a ferromagnetic NiFe thin film due to an adjacent  $\alpha$ -Sn thin film. Ferromagnetic resonance studies show that an  $\alpha$ -Sn film separated from a NiFe film by an ultrathin Ag spacer can cause an extra damping in the NiFe film that is three times bigger than the intrinsic damping of the NiFe film. Such an extra damping is absent in structures where the  $\alpha$ -Sn film interfaces directly with a NiFe film, or is replaced by a  $\beta$ -Sn film. The data suggest that the extra damping is associated with topologically nontrivial surface states in the topological Dirac semimetal phase of the  $\alpha$ -Sn film. This work suggests that, like topological insulators, topological Dirac semimetal  $\alpha$ -Sn may have promising applications in spintronics.

## 1. Introduction

The phenomenon of spin pumping refers to the transfer of spins from precessional moments in a ferromagnet to a nonmagnetic material.<sup>[1–3]</sup> In a ferromagnetic/nonmagnetic bilayered system, spin pumping manifests itself as two distinct effects: 1) an enhancement in the damping in the ferromagnetic

layer and 2) a pure spin current in the nonmagnetic layer. The strength of these effects usually depends on the spin–orbit coupling (SOC) in the nonmagnetic layer. This is because spin pumping creates a spin chemical potential gradient across the thickness of the nonmagnetic layer, which drives a backflow spin current into the ferromagnet and thereby compensates partially the loss due to the spin pumping.<sup>[4]</sup> The size of the spin chemical potential gradient is directly determined by the spin-flip processes in the nonmagnetic layer, while the latter usually depends on the SOC, as discussed in the Supporting Information.

As such, the spin-pumping effects are usually weak if the nonmagnetic layer is a metallic thin film with weak SOC, such as Cu and Ag, but can be very strong if the nonmagnetic layer is a heavy metal thin film with strong SOC, such as Pt and W.<sup>[5–8]</sup> The effects can be even stronger if the nonmagnetic component is a topological insulator (TI), such as Bi<sub>2</sub>Se<sub>3</sub> and SmB<sub>6</sub>.<sup>[9–13]</sup> Topological surface states in a TI exhibit intrinsic spin-momentum locking, which is an extreme example of strong SOC.<sup>[14]</sup>

Topological surface states (TSS) should also be present in other topological materials, such as Dirac semimetals and Weyl semimetals. Such states should appear at, for example, the interface in a ferromagnet/topological semimetal layered structure, due to the difference in the band topologies of the two types of materials. These TSS are also expected to exhibit spin-momentum locking due to the broken inversion symmetry at the interface. As such, one may also expect strong spin pumping in layered ferromagnet/Dirac semimetal systems.

This letter reports on the experimental observation of strong spin pumping in a ferromagnetic thin film due to TSS in a neighboring Dirac semimetal  $\alpha$ -Sn thin film. It is known that unstrained  $\alpha$ -Sn is a zero-gap semiconductor in which the conduction and valence bands have quadratic band touching at the  $\Gamma$  point at the Fermi level. This quadratic touching is protected by the cubic symmetry of the  $\alpha$ -Sn crystalline structure. However, when the cubic symmetry is broken by a tensile strain along the [001] or [111] direction, the conduction and valence bands cross each other near the Fermi level, forming two Dirac points with linear dispersion and giving rise to a topological Dirac semimetal (TDS) phase.<sup>[15–17]</sup> Such band crossing is protected by the rotational symmetry that remains unbroken by the strain. In **Figure 1**, this band crossing is shown by the crossing

Dr. J. Ding, Dr. C. Liu, Y. Zhang, Dr. V. Kalappattil, Dr. R. Yu,  
Prof. H. Chen, Prof. M. Wu  
Department of Physics  
Colorado State University  
Fort Collins, CO 80523, USA  
E-mail: mww@colostate.edu

Y. Zhang  
School of Optical and Electronic Information  
Huazhong University of Science and Technology  
Wuhan, Hubei 430074, China

Dr. R. Yu, Prof. H. Ding  
National Laboratory of Solid State Microstructures and Department  
of Physics

Nanjing University  
Nanjing, Jiangsu 210093, China

U. Erugu, Prof. J. Tang  
Department of Physics and Astronomy  
University of Wyoming  
Laramie, Wyoming 82071, USA

Prof. H. Chen  
School of Advanced Materials Discovery  
Colorado State University  
Fort Collins, CO 80523, USA

 The ORCID identification number(s) for the author(s) of this article can be found under <https://doi.org/10.1002/adfm.202008411>.

DOI: 10.1002/adfm.202008411

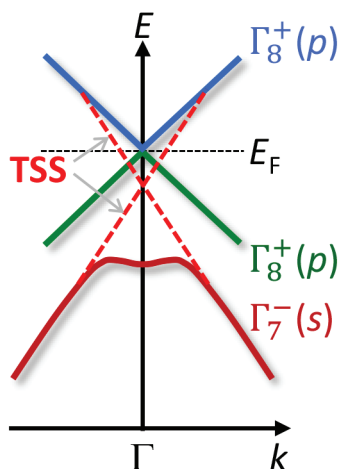


**Figure 1.** Schematic of band structure in topological Dirac semimetal  $\alpha$ -Sn.<sup>[15,16]</sup>

of the blue and green lines at the Fermi level, and the crossing point represents one of the two Dirac points.

The TSS of the TDS  $\alpha$ -Sn film concerned in this work originates from the band inversion—the conduction and valence bands ( $\Gamma_8^+$ ) near the Fermi level are derived from p electrons whereas the s-derived band ( $\Gamma_7^-$ ) is below the Fermi level, as sketched in Figure 1, unlike other group-IV semiconductors with the diamond structure such as Si and Ge. The  $\Gamma_7^-$  band is pushed below the Fermi level mainly due to the scalar relativistic effects that affect the s electrons.<sup>[18,19]</sup> The TSS bridge the  $\Gamma_8^+$  conduction band and the  $\Gamma_7^-$  valence band,<sup>[15,16]</sup> as indicated by the red dashed lines in Figure 1. Note that these TSS are different from Fermi arc states in  $\alpha$ -Sn thin films, as discussed shortly.

In this work, TDS  $\alpha$ -Sn thin films are realized by the use of single-crystal InSb substrates. The lattice constant of  $\alpha$ -Sn ( $a = 6.489 \text{ \AA}$ ) is slightly larger than that of InSb ( $a = 6.479 \text{ \AA}$ ), and this lattice mismatching gives rise to an in-plane compressive strain or a perpendicular tensile strain in the  $\alpha$ -Sn films.<sup>[15,20,21]</sup> The work made use of layered  $\alpha$ -Sn(6 nm)/Ag(2 nm)/NiFe(20 nm) structures where the NiFe film is ferromagnetic, and the nonmagnetic Ag layer works as a spacer to physically separate  $\alpha$ -Sn and NiFe and thereby avoid the suppression of TSS in  $\alpha$ -Sn by the magnetic ordering in the NiFe film. The damping in these structures is found to be a factor of about 4.8 bigger than in the single-layer NiFe film. Control measurements indicate that this damping enhancement is mostly due to the TSS in the  $\alpha$ -Sn film, rather than the bulk

of the  $\alpha$ -Sn film or the Ag spacer; it is absent in  $\beta$ -Sn(6 nm)/Ag(2 nm)/NiFe(20 nm) where the  $\beta$ -Sn film is topologically trivial.

Three important points should be highlighted. First, the TDS is a relatively newly discovered topological phase. In comparison with other known TDS materials,<sup>[22–25]</sup>  $\alpha$ -Sn is more appealing for two reasons. i) It is a single-element material and is therefore relatively easy to grow. ii) It can transform into other topological phases, such as a TI and a Weyl semimetal, under certain strains or magnetic fields<sup>[15–17]</sup> and therefore represents an ideal platform for exploring effects of topological phase transition on spintronic properties. Second, this work suggests that TDS materials may be as promising as TI materials in terms of applications in spintronics. Third, the  $\alpha$ -Sn films in this work were grown by sputtering, which is an industry-friendly thin film growth technique.

## 2. Results and Discussions

The  $\alpha$ -Sn films were grown on (001) InSb substrates by sputtering, as described in the Supporting Information. **Figure 2** presents the structural properties of an 8-nm-thick  $\alpha$ -Sn film. Figure 2a,b gives a wide-angle X-ray diffraction (XRD) spectrum and a fine-scan XRD spectrum, respectively. The dotted and dashed vertical lines in Figure 2b indicate the expected positions for the  $\alpha$ -Sn (004) and InSb (004) peaks, respectively. The red curve in Figure 2b is a fit that consists of three Voigt functions: one for the  $\alpha$ -Sn (004) peak and the other two for the InSb (004) peaks. Figure 2c shows an atomic force microscopy (AFM) surface image; the indicated roughness value is determined by averaging over AFM measurements on five different  $5 \mu\text{m} \times 5 \mu\text{m}$  areas; the uncertainty is the corresponding standard deviation.

Four results are evident from the data in Figure 2. 1) Although  $\alpha$ -Sn and  $\beta$ -Sn coexist, the  $\alpha$  phase is overwhelmingly dominant over the  $\beta$  phase. Specifically, the fitting analysis shows that the  $\alpha$ -Sn (004) peak has an XRD intensity of almost 100 times stronger than the  $\beta$ -Sn (002) peak (see Figure S1, Supporting Information). 2) There is only one peak for the  $\alpha$ -Sn, indicating the highly epitaxial growth of the film. 3) The  $\alpha$ -Sn (004) peak appears on the left side of the expected peak position, which indicates the presence of a perpendicular tensile strain or an elongation along the perpendicular direction in the film. This is consistent with the expectation—the  $\alpha$ -Sn film grown on the InSb substrate should exhibit an in-plane compressive strain because the lattice constant of  $\alpha$ -Sn is slightly

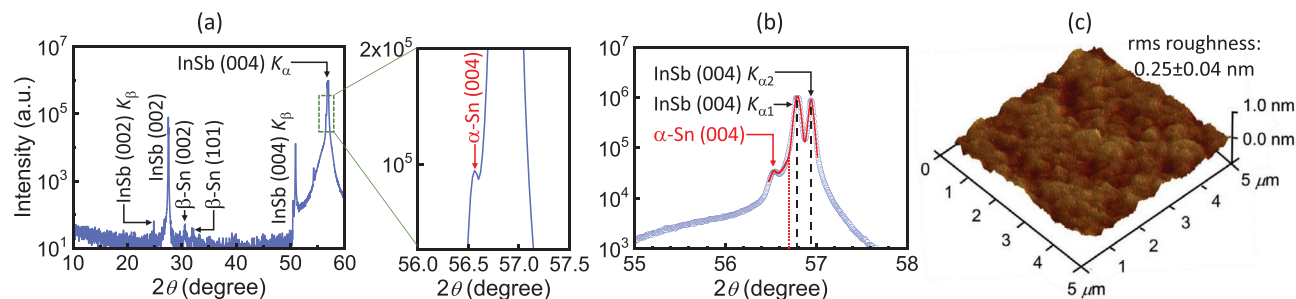


**Figure 2.** Properties for a 8-nm-thick  $\alpha$ -Sn film grown on a (001) InSb substrate. a) X-ray diffraction spectrum (XRD). b) Fine-scan XRD spectrum. c) Atomic force microscopy surface image.

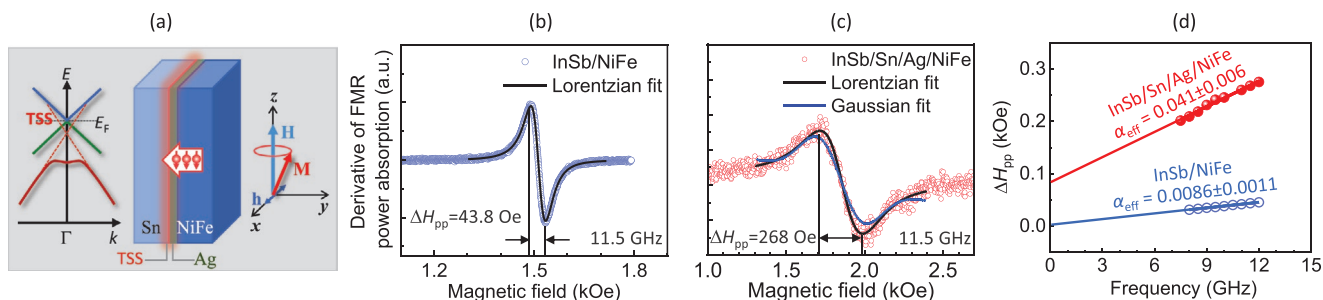


**Figure 3.** TSS-enhanced spin pumping in  $\alpha$ -Sn/NiFe structures. a) Conceptual diagram. b) FMR profile of InSb/NiFe(20 nm). c) FMR profile of InSb/ $\alpha$ -Sn(6 nm)/Ag(2 nm)/NiFe(20 nm). d) FMR linewidth as a function of frequency for the two samples.

larger than that of InSb.<sup>[15,20,21]</sup> The Voigt fitting yields  $a = 6.489 \pm 0.005 \text{ \AA}$  for the  $\alpha$ -Sn film, which corresponds to a tensile strain of  $(0.27 \pm 0.08)\%$ . Such a strain makes the  $\alpha$ -Sn film a TDS.<sup>[15–17]</sup> 4) The film has a very smooth surface, with a roughness of only about 0.25 nm. This smooth surface facilitates the fabrication of heterostructures with high-quality interfaces for spin-pumping studies.

Two points should be noted about the properties of the  $\alpha$ -Sn film. First, the electronic band structure of (001)  $\alpha$ -Sn films grown on (001) InSb substrates has been previously characterized by separate research groups, using angle-resolved photoemission microscopy (ARPES).<sup>[10,26,27]</sup> As the  $\alpha$ -Sn films in this work were also grown on (001) InSb substrates and show the same crystalline structure, one can expect similar electronic band properties in the films. Future work is of great interest that makes use of ARPES measurements to confirm this expectation. Second, while not presented here, electrical transport measurements have been carried out on the  $\alpha$ -Sn thin films; the films show electrical properties expected for Dirac semimetals.<sup>[28]</sup>

**Figure 3** shows the main results of this work. Figure 3a illustrates the spin-pumping process in an  $\alpha$ -Sn/Ag/NiFe layered structure. In brief, a microwave magnetic field ( $\mathbf{h}$ ) can drive the magnetization ( $\mathbf{M}$ ) in the NiFe film to precess around the static field ( $\mathbf{H}$ ); this precession can pump a spin current that flows across the Ag spacer and then enters the  $\alpha$ -Sn film.<sup>[1–3]</sup> Due to spin-momentum locking of the TSS, the  $\alpha$ -Sn film can work as a highly efficient spin absorber, leading to a very weak spin backflow; the net effect is an additional damping to the damping ( $\alpha_0$ ) of the NiFe film, which is evidently indicated by the ferromagnetic resonance (FMR) data presented in Figure 3b–d.

Figure 3b,c shows the FMR data measured on an InSb/NiFe(20 nm) sample and an InSb/ $\alpha$ -Sn(6 nm)/Ag(2 nm)/NiFe(20 nm) sample, respectively, at a frequency of  $f = 11.5 \text{ GHz}$  with an X-band shorted waveguide.<sup>[29]</sup> The symbols show the data, while the curves are fits to Lorentzian and Gaussian functions. The fitting-yielded peak-to-peak FMR linewidth ( $\Delta H_{pp}$ ) values are indicated. Note that the NiFe films in this work are 20-nm-thick Ni<sub>80</sub>Fe<sub>20</sub> films; they were grown with the same target and the same sputtering process.

The data in Figure 3b,c show that the FMR in the InSb/ $\alpha$ -Sn/Ag/NiFe sample is significantly broader than that in the InSb/NiFe sample. Specifically,  $\Delta H_{pp}$  in InSb/ $\alpha$ -Sn/Ag/NiFe is more than six times larger than that in InSb/NiFe. Further, Figure 3c shows that the Lorentzian fit is much better than the Gaussian fit, indicating that the film inhomogeneity contribution to  $\Delta H_{pp}$  is relatively small.<sup>[30]</sup> These results together

suggest that a significant damping due to spin pumping is present in the sample with an  $\alpha$ -Sn layer, as discussed shortly.

To confirm the above-discussed,  $\alpha$ -Sn-produced linewidth broadening, FMR measurements were repeated at different frequencies ( $f$ ). The resulting  $\Delta H_{pp}$  versus  $f$  responses are shown in Figure 3d. One can see that  $\Delta H_{pp}$  in the sample with an  $\alpha$ -Sn layer is larger at all frequencies, confirming the result shown in Figure 3b,c. The lines in Figure 3d show fits to

$$\Delta H_{pp} = \frac{2\alpha_{\text{eff}}}{\sqrt{3}|\gamma|} f + \Delta H_0 \quad (1)$$

where  $\alpha_{\text{eff}}$  is the effective damping constant,  $|\gamma| = 2.8 \text{ MHz/Oe}$  is the absolute gyromagnetic ratio, and  $\Delta H_0$  denotes the inhomogeneity-caused line broadening.<sup>[30]</sup> The fitting-yielded  $\alpha_{\text{eff}}$  values are indicated in the figure. One can see that  $\alpha_{\text{eff}}$  in the sample with the  $\alpha$ -Sn film is about 380% larger (or about a factor of 4.8 bigger) than that in the one without an  $\alpha$ -Sn film.

Two points should be made about the FMR data presented in Figure 3. First, the inhomogeneity line broadening in the NiFe films is relatively small. This result is derived from three observations as follows: 1) The experimental FMR profiles can be nicely fitted by the derivative of a Lorentzian function, as shown representatively in Figure 3b. 2) The Lorentzian function fits the FMR profiles better than the Gaussian function, as shown in Figure 3c. Note that in the case of strong inhomogeneity, a Gaussian function would fit the FMR profile better than a Lorentzian function. 3)  $\Delta H_0$  is notably smaller than  $\Delta H_{pp}$ , as shown in Figure 3d. For example, the InSb/NiFe sample shows  $\Delta H_0 = 0.003 \text{ kOe}$  and  $\Delta H_{pp} = 0.040 \text{ kOe}$  at 10 GHz, with the former being only 75% of the latter. The second point is that two-magnon scattering in the NiFe films is expected to be weak. The main justification for this is that the damping constant (0.0086) of the NiFe film is consistent with the values (0.007–0.01) reported previously for high-quality NiFe thin films.<sup>[31–33]</sup> The other two justifications are that 1) the two  $\Delta H_{pp}$  versus  $f$  responses shown in Figure 3d are both linear, and the linear fitting-yielded  $\alpha_{\text{eff}}$  uncertainties are much smaller than the  $\alpha_{\text{eff}}$  values, and 2) the damping of the NiFe film exhibits weak dependence on the crystalline and microstructural properties of the material on which the film was grown, as shown in Section S7 of Supporting Information.

The data in Figure 3 evidently show that the damping in the InSb/ $\alpha$ -Sn/Ag/NiFe structure is substantially larger than that in the InSb/NiFe sample. The large damping in InSb/ $\alpha$ -Sn/Ag/NiFe, however, is not solely due to the  $\alpha$ -Sn layer, but also includes a contribution from spin absorption in the Ag spacer.

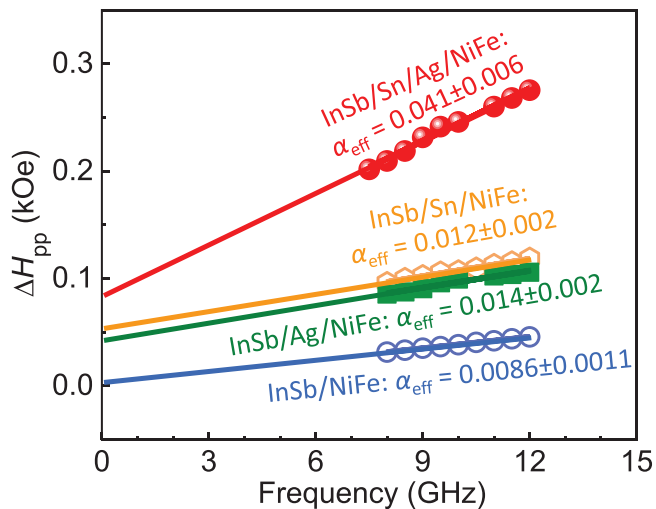


**Figure 4.** Comparison of FMR linewidth versus frequency responses measured on four different samples, as indicated.

Approximately, the damping in InSb/ $\alpha$ -Sn/Ag/NiFe can be written as

$$\alpha_{\text{eff}} = \alpha_0 + \alpha_{\text{Ag}} + \alpha_{\text{Sn}} \quad (2)$$

where  $\alpha_0 = 0.0086 \pm 0.0011$  is the damping in the NiFe film, and  $\alpha_{\text{Ag}}$  and  $\alpha_{\text{Sn}}$  denote the extra damping in the NiFe film due to the spin absorption in the Ag and Sn layers, respectively. From Equation (2), one obtains  $\alpha_{\text{Ag}} + \alpha_{\text{Sn}} = \alpha_{\text{eff}} - \alpha_0 \approx 0.0324$ , but the weight of  $\alpha_{\text{Sn}}$  in the overall damping enhancement is unclear.

In order to determine  $\alpha_{\text{Sn}}$ , a control sample InSb/Ag(2 nm)/NiFe(20 nm) was fabricated using exactly the same substrate, targets, and sputtering process as for the InSb/ $\alpha$ -Sn(6 nm)/Ag(2 nm)/NiFe(20 nm) sample, and the same FMR measurements were conducted on this control sample. The green symbols in **Figure 4** show the measured data. The fitting yields  $\alpha_{\text{eff}} = 0.014 \pm 0.002$ . If one considers  $\alpha_{\text{eff}} = \alpha_0 + \alpha_{\text{Ag}}$  in this sample, one obtains  $\alpha_{\text{Ag}} \approx 0.0054$ .

With  $\alpha_{\text{Ag}}$  being determined, one can now use Equation (2) to find  $\alpha_{\text{Sn}} = \alpha_{\text{eff}} - \alpha_0 - \alpha_{\text{Ag}} \approx 0.027$ . Thus, one can see two important results. First,  $\alpha_{\text{Ag}}$  is relatively small in comparison with  $\alpha_0$  in the NiFe film. This is consistent with the expectation, namely, that the Ag layer works as a poor spin sink or a good spin conductor because it has relatively weak SOC. It is for the same reason that Ag is chosen as a spacer material in this work. Note that the spin Hall angle in Ag is  $\sim 0.0068$  only, while the spin diffusion length in Ag is  $\approx 700$  nm,<sup>[34]</sup> which is much bigger than the Ag thickness in this work. Second,  $\alpha_{\text{Sn}}$  is remarkably bigger—it is more than 3 times bigger than  $\alpha_0$  and about 5 times bigger than  $\alpha_{\text{Ag}}$ . This clearly indicates the presence of very strong SOC in the  $\alpha$ -Sn film. As discussed early in the introduction, the stronger SOC the nonmagnetic layer has, the larger damping enhancement the spin pumping causes.

The above-determined  $\alpha_{\text{Sn}}$  is independent of the nature of the Ag/NiFe interface, because the Ag/NiFe interface is present in both the InSb/ $\alpha$ -Sn/Ag/NiFe and InSb/Ag/NiFe samples and its effects on the damping have already been accounted for

by  $\alpha_{\text{Ag}}$ . One can therefore attribute  $\alpha_{\text{Sn}}$  to the 2D TSS at the  $\alpha$ -Sn/Ag interface or the SOC in the bulk of the  $\alpha$ -Sn film. To check the possibility of the bulk SOC origin, a control sample InSb/ $\alpha$ -Sn(6 nm)/NiFe(20 nm) was prepared using exactly the same growth conditions as the InSb/ $\alpha$ -Sn(6 nm)/Ag(2 nm)/NiFe(20 nm) sample. It is expected that the  $\alpha$ -Sn TSS in this control sample are suppressed or damaged due to direct physical contact with the NiFe film; the main reason for such suppression is that the proximity to the magnetic ordering in the NiFe film breaks the time-reversal symmetry of the TSS.<sup>[10]</sup> Previous experimental and theoretical works have shown that the magnetism in a ferromagnetic metal can significantly modify and even completely suppress TSS in a neighboring TI or  $\alpha$ -Sn thin film.<sup>[10,35–38]</sup>

The orange symbols in **Figure 4** present the  $\Delta H_{\text{pp}}$  data measured on the InSb/ $\alpha$ -Sn/NiFe control sample in which TSS are expected to be absent. The fitting yields  $\alpha_{\text{eff}} = 0.012 \pm 0.002$ , which indicates  $\alpha_{\text{Sn}} \approx 0.0034$ . Thus, one can see that the  $\alpha_{\text{Sn}}$  value (0.0034) in the InSb/ $\alpha$ -Sn/NiFe sample, where only the bulk states contribute to spin absorption, is only about 13% of the  $\alpha_{\text{Sn}}$  value (0.0027) in the InSb/ $\alpha$ -Sn/Ag/NiFe sample, where both the bulk states and the TSS contribute. This big difference evidently shows that the large  $\alpha_{\text{Sn}}$  in the InSb/ $\alpha$ -Sn/Ag/NiFe sample is mostly due to the TSS, while the bulk contribution is relatively small.

It should be highlighted that the topological nature of the  $\alpha$ -Sn film plays a critical role in the strong damping enhancement. To demonstrate this role, a control sample Al<sub>2</sub>O<sub>3</sub>/Sn(6 nm)/Ag(2 nm)/NiFe(20 nm) was fabricated using the same conditions as for the InSb/ $\alpha$ -Sn(6 nm)/Ag(2 nm)/NiFe(20 nm) sample, but with a different substrate. Note that the two samples were prepared using exactly the same targets and exactly the same sputtering process. The only difference was the substrate: one was grown on a (0001) Al<sub>2</sub>O<sub>3</sub> substrate, whereas the other was on a (001) InSb substrate. **Figure 5** shows the data on this sample. The XRD spectrum shows that the Sn film grown on a sapphire substrate has  $\beta$  phase, rather than  $\alpha$  phase. This results from the fact that the sapphire has a crystalline structure very different from the  $\alpha$ -Sn, and the  $\beta$ -Sn film on the sapphire is more stable at room temperature (see the Supporting Information). The green symbols in **Figure 5b** show the  $\Delta H_{\text{pp}}$  data of the Al<sub>2</sub>O<sub>3</sub>/Sn/Ag/NiFe sample. The fitting yields  $\alpha_{\text{eff}} = 0.019 \pm 0.001$ . Based on this value and Equation (2), one obtains  $\alpha_{\text{Sn}} \approx 0.005$ . One can see that  $\alpha_{\text{Sn}}$  in the sample with  $\beta$ -Sn is only  $\approx 17\%$  of that in the sample with  $\alpha$ -Sn. This is in agreement with the expectation— $\beta$ -Sn is topologically trivial<sup>[39]</sup> and there exist no spin-momentum-locked TSS at the  $\beta$ -Sn/Ag interface, giving rise to weak spin absorption in the  $\beta$ -Sn.

In order to describe more quantitatively the strong spin absorption in  $\alpha$ -Sn/Ag/NiFe, one can define an effective spin mixing conductance  $g_{\uparrow\downarrow}^{\text{eff}}$  as<sup>[40,41]</sup>

$$\text{Re}(g_{\uparrow\downarrow}^{\text{eff}}) = \frac{4\pi M_s d}{h|\gamma|} (\alpha_{\text{eff}} - \alpha_0) \quad (3)$$

where “Re” denotes the real part of  $g_{\uparrow\downarrow}^{\text{eff}}$ ,  $4\pi M_s \approx 784$  kG is the saturation induction of the NiFe film (see the Supporting Information),  $d = 20$  nm is the NiFe thickness, and  $\hbar$

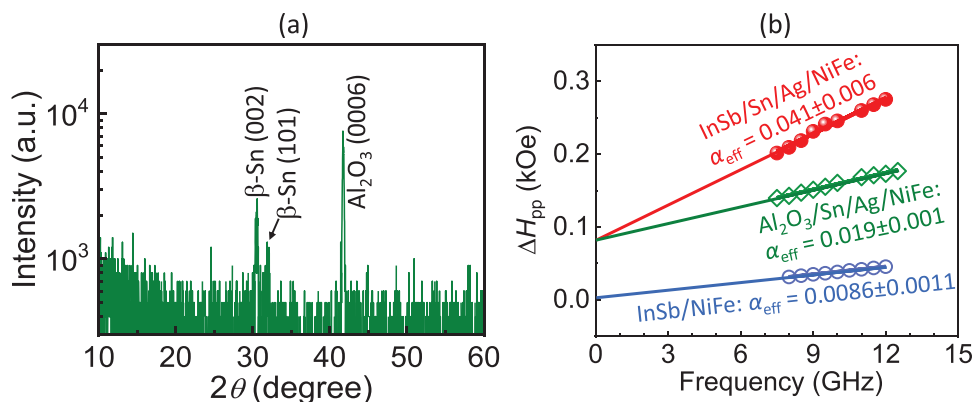


**Figure 5.** a) XRD spectrum of an 8-nm-thick  $\beta$ -Sn film grown on a (0001) sapphire substrate. b) Comparison of the FMR linewidth versus frequency responses of the  $\text{Al}_2\text{O}_3/\text{Sn}$  (6 nm)/Ag(2 nm)/NiFe(20 nm) sample and the other two samples.

is the reduced Planck constant. The calculation using Equation (3),  $|\gamma| = 2.8 \text{ MHz/Oe}$ ,  $\alpha_0 = 0.0086$ , and  $\alpha_{\text{eff}} = 0.041$  yields  $\text{Re}(g_{\uparrow\downarrow}^{\text{eff}}) = 2.7 \times 10^{16} \text{ cm}^{-2}$ . This value is about one order of magnitude larger than the values in systems where spin absorption is attributed to SOC in heavy metals<sup>[40]</sup> or at Rashba interfaces.<sup>[41]</sup> This large value is mostly due to the large spin absorption associated with the spin-momentum-locked TSS. Note that a part of this large value may come from the film inhomogeneity. The presence of inhomogeneity-caused FMR linewidth broadening makes the extraction of  $g_{\uparrow\downarrow}^{\text{eff}}$  challenging; it cannot be excluded that areas with slightly different  $4\pi M_s$  or anisotropy lead to different FMR fields and thereby make the derivation of  $g_{\uparrow\downarrow}^{\text{eff}}$  from the slopes of the  $\Delta H_{\text{pp}}$  versus  $f$  responses less precise.

Three notes should be made. First, the data in Figures 4 and 5b for the InSb/NiFe and InSb/ $\alpha$ -Sn/NiFe samples are the same as those shown in Figure 3d. They are included to ease comparison between the different samples. Second, the fitting of the FMR field versus  $f$  data to the Kittel equation yields  $|\gamma| = 2.73 \text{ MHz/Oe}$  (see the Supporting Information), which is only 2.5% smaller than the  $|\gamma|$  values used in the above analyses. Analyses using this  $|\gamma|$  value gave the results that are only slightly different. In the above analysis the standard  $|\gamma|$  value was chosen intentionally to ease comparison of  $\text{Re}(g_{\uparrow\downarrow}^{\text{eff}})$  in different materials. Third, in this work the FMR measurements made use of low microwave power and the FMR studies were therefore carried out in a linear regime. The analyses may be inappropriate if one works in a nonlinear regime.

Several final remarks are as follows:

- 1) The  $\alpha$ -Sn films in this work are all 6-nm thick. In thicker films, the  $\beta$  phase may be dominant over the  $\alpha$  phase (see Section S3, Supporting Information). On the other hand, with reduced  $\alpha$ -Sn thicknesses, the quantum confinement effect may turn a TDS to a TI or a quantum spin Hall insulator.<sup>[42–45]</sup>
- 2) Previous work has shown that interfacing a TI with a ferromagnet can damage or suppress the TSS in the TI.<sup>[10,35–38]</sup> The comparison between the damping of the InSb/ $\alpha$ -Sn/Ag/NiFe and InSb/ $\alpha$ -Sn/NiFe samples in Figure 4 evidently suggests that this is also the case for the TSS in the TDS  $\alpha$ -Sn.
- 3) TDSs should also host Fermi arc surface states;<sup>[46,47]</sup> in the case of TDS  $\alpha$ -Sn, such states are expected to exist on surfaces parallel to the uniaxial tensile axis,<sup>[16]</sup> namely, the four side

surfaces of the  $\alpha$ -Sn film in this work. Future studies on spin pumping effects associated with these surface states are very interesting.

- 4) This work suggests that SOC in the bulk of  $\alpha$ -Sn and  $\beta$ -Sn films is no stronger than that in Ag. Future work is of great interest that evaluates the bulk SOC strength, such as the spin Hall angle, in  $\alpha$ -Sn and  $\beta$ -Sn films via, for example, spin-torque FMR experiments. Future work is also worthy that studies the effects of the Ag spacer thickness and the interface quality on the spin pumping.
- 5) As pointed out earlier, a TDS  $\alpha$ -Sn can undergo a topological phase transition under certain conditions, transforming, for example, to a TI  $\alpha$ -Sn.<sup>[15–17]</sup> A previous work has studied damping enhancement due to TSS in the TI phase of  $\alpha$ -Sn.<sup>[10]</sup> One significant difference of this work from the previous work is the use of a sequence of carefully designed samples to conclusively separate and confirm the role of the TSS in the damping enhancement, as well as the role of the topology. The other major differences include i) the  $\alpha$ -Sn films in the previous work were grown by molecular-beam epitaxy (MBE), while the  $\alpha$ -Sn films in this work were grown by sputtering. Because sputtering is much more industry friendly than the MBE technique, this work is of great technological significance. ii) In spite of the fact that the films were grown by sputtering, the interfaces are of high quality in terms of spin transfer efficiency. Specifically, the structures in this work show  $\text{Re}(g_{\uparrow\downarrow}^{\text{eff}}) = 2.7 \times 10^{16} \text{ cm}^{-2}$ , which is about 3.9 times larger than the value ( $0.7 \times 10^{16} \text{ cm}^{-2}$ ) reported by Rojas-Sánchez et al.<sup>[10]</sup> iii) In addition to the technological significance highlighted above, the existence of TSS in polycrystalline  $\alpha$ -Sn films grown by sputtering has fundamental significance. This is because the topological classification of materials is almost exclusively based on crystal Hamiltonians, and there are very few evidences on the existence of TSS in materials that are not single crystals. In other words, the sputtered  $\alpha$ -Sn thin films in this work represent an important model system for understanding material topology beyond single crystals.
- 6) The presented damping and spin mixing conductance enhancement induced by TSS in TDS  $\alpha$ -Sn films is as significant as that induced by TSS in TI materials.<sup>[9–13]</sup> This result, together with efficient magnetization switching

induced by TSS in TDS  $\alpha$ -Sn films,<sup>[28]</sup> evidently show that TDS  $\alpha$ -Sn may be as promising as TI materials in terms of spintronic applications.

### 3. Conclusions

In summary, ferromagnetic resonance studies reveal that a thin film of topological Dirac semimetal  $\alpha$ -Sn can significantly enhance the damping in a neighboring ferromagnetic thin film. Measurements on a sequence of control samples show that this damping enhancement is not associated with the spin-orbit coupling in the bulk of the  $\alpha$ -Sn film, but is due to the topological surface states in the  $\alpha$ -Sn film; it is absent when the  $\alpha$ -Sn film is replaced by a thin film of  $\beta$ -Sn, which is a topologically trivial metal. This work suggests that, like topological insulators,  $\alpha$ -Sn in the topological Dirac semimetal phase may have broad applications in spintronics.

### Supporting Information

Supporting Information is available from the Wiley Online Library or from the author.

### Acknowledgements

This work was supported by the U.S. Department of Energy, Office of Science, Basic Energy Sciences (DE-SC0018994). The fabrication and characterization of control samples without Sn films were supported by the U.S. National Science Foundation (EFMA-1641989 and ECCS-1915849). Work at NJU was supported by the National Natural Science Foundation of China (11734006 and 11974165). Work at UW was supported by the U.S. National Science Foundation (DMR-1710512). The authors thank Albert Fert and Laurent Vila for valuable suggestions.

### Conflict of Interest

The authors declare no conflict of interest.

### Keywords

ferromagnetic resonance, magnetic damping, spin pumping, topological Dirac semimetals, topological quantum materials, topological surface states

Received: October 2, 2020  
Revised: December 11, 2020  
Published online:

- [1] B. Heinrich, J. A. C. Bland, *Ultrathin Magnetic Structures: Fundamentals of Nanomagnetism*, Springer, Berlin **2005**.  
[2] R. Urban, G. Woltersdorf, B. Heinrich, *Phys. Rev. Lett.* **2001**, *87*, 217204.  
[3] Y. Tserkovnyak, A. Brataas, G. E. W. Bauer, *Phys. Rev. Lett.* **2002**, *88*, 117601.

- [4] Y. Tserkovnyak, A. Brataas, G. E. W. Bauer, B. I. Halperin, *Rev. Mod. Phys.* **2005**, *77*, 1375.  
[5] C. W. Sandweg, Y. Kajiwara, K. Ando, E. Saitoh, B. Hillebrands, *Appl. Phys. Lett.* **2010**, *97*, 252504.  
[6] O. Mosendz, V. Vlaminck, J. E. Pearson, F. Y. Fradin, G. E. W. Bauer, S. D. Bader, A. Hoffmann, *Phys. Rev. B* **2010**, *82*, 214403.  
[7] C. W. Sandweg, Y. Kajiwara, A. V. Chumak, A. A. Serga, V. I. Vasyuchka, M. B. Jungfleisch, E. Saitoh, B. Hillebrands, *Phys. Rev. Lett.* **2011**, *106*, 216601.  
[8] Z. Duan, C. T. Boone, X. Cheng, I. N. Krivorotov, *Phys. Rev. B* **2014**, *90*, 024427.  
[9] Q. Song, J. Mi, D. Zhao, T. Su, W. Yuan, W. Xing, Y. Chen, T. Wang, T. Wu, X. H. Chen, X. C. Xie, C. Zhang, J. Shi, W. Han, *Nat. Commun.* **2016**, *7*, 13485.  
[10] J.-C. Rojas-Sánchez, S. Oyarzún, Y. Fu, A. Marty, C. Vergnaud, S. Gambarelli, L. Vila, M. Jamet, Y. Ohtsubo, A. Taleb-Ibrahimi, P. Le Fèvre, F. Bertran, N. Reyren, J.-M. George, A. Fert, *Phys. Rev. Lett.* **2016**, *116*, 096602.  
[11] C. Tang, Q. Song, C.-Z. Chang, Y. Xu, Y. Ohnuma, M. Matsuo, Y. Liu, W. Yuan, Y. Yao, J. S. Moodera, S. Maekawa, W. Han, J. Shi, *Sci. Adv.* **2018**, *4*, 8660.  
[12] Y. T. Fanchiang, K. H. M. Chen, C. C. Tseng, C. C. Chen, C. K. Cheng, C. N. Wu, S. F. Lee, M. Hong, J. Kwo, *Nat. Commun.* **2018**, *9*, 223.  
[13] H. Wang, J. Kally, C. Şahin, T. Liu, W. Yanez, E. J. Kamp, A. Richardella, M. Wu, M. E. Flatté, N. Samarth, *Phys. Rev. Res.* **2019**, *1*, 012014(R).  
[14] F. Hellman, A. Hoffmann, Y. Tserkovnyak, G. S. Beach, E. E. Fullerton, C. Leighton, A. H. MacDonald, D. C. Ralph, D. A. Arena, H. A. Dürr, P. Fischer, *Rev. Mod. Phys.* **2017**, *89*, 025006.  
[15] C.-Z. Xu, Y.-H. Chan, Y. Chen, P. Chen, X. Wang, C. Dejoie, M.-H. Wong, J. A. Hlevyack, H. Ryu, H.-Y. Kee, N. Tamura, M.-Y. Chou, Z. Hussain, S.-K. Mo, T.-C. Chiang, *Phys. Rev. Lett.* **2017**, *118*, 146402.  
[16] H. Huang, F. Liu, *Phys. Rev. B* **2017**, *95*, 201101(R).  
[17] D. Zhang, H. Wang, J. Ruan, G. Yao, H. Zhang, *Phys. Rev. B* **2018**, *97*, 195139.  
[18] S. C. Zhang, X. L. Qi, *Phys. Today* **2010**, *63*, 12.  
[19] Z. Zhu, Y. Cheng, U. Schwingenschlögl, *Phys. Rev. B* **2012**, *85*, 235401.  
[20] H. Song, J. Yao, Y. Ding, Y. Gu, Y. Deng, M.-H. Lu, H. Lu, Y.-F. Chen, *Adv. Eng. Mater.* **2019**, *21*, 1900410.  
[21] I. Madarevic, U. Thupakula, G. Lippertz, N. Claessens, P.-C. Lin, H. Bana, S. Gonzalez, G. D. Santo, L. Petaccia, M. N. Nair, L. M. C. Pereira, C. V. Haesendonck, M. J. Van Bael, *APL Mater.* **2020**, *8*, 031114.  
[22] C.-Z. Li, L.-X. Wang, H. Liu, J. Wang, Z.-M. Liao, D.-P. Yu, *Nat. Commun.* **2015**, *6*, 10137.  
[23] H. Li, H. He, H.-Z. Lu, H. Zhang, H. Liu, R. Ma, Z. Fan, S.-Q. Shen, J. Wang, *Nat. Commun.* **2016**, *7*, 10301.  
[24] C. Zhang, E. Zhang, W. Wang, Y. Liu, Z.-G. Chen, S. Lu, S. Liang, J. Cao, X. Yuan, L. Tang, Q. Li, C. Zhou, T. Gu, Y. Wu, J. Zou, F. Xiu, *Nat. Commun.* **2017**, *8*, 13741.  
[25] Y. Zhang, C. Wang, L. Yu, G. Liu, A. Liang, J. Huang, S. Nie, X. Sun, Y. Zhang, B. Shen, J. Liu, H. Weng, L. Zhao, G. Chen, X. Jia, C. Hu, Y. Ding, W. Zhao, Q. Gao, C. Li, S. He, L. Zhao, F. Zhang, S. Zhang, F. Yang, Z. Wang, Q. Peng, X. Dai, Z. Fang, Z. Xu, C. Chen, X. J. Zhou, *Nat. Commun.* **2017**, *8*, 15512.  
[26] A. Barfuss, L. Dudy, M. R. Scholz, H. Roth, P. Höpfner, C. Blumenstein, G. Landolt, J. H. Dil, N. C. Plumb, M. Radovic, A. Bostwick, E. Rotenberg, A. Fleszar, G. Bihlmayer, D. Wortmann, G. Li, W. Hanke, R. Claessen, J. Schäfer, *Phys. Rev. Lett.* **2013**, *111*, 157205.  
[27] Y. Ohtsubo, P. Le Fèvre, F. Bertran, A. Taleb-Ibrahimi, *Phys. Rev. Lett.* **2013**, *111*, 216401.  
[28] J. Ding, C. Liu, V. Kalappattil, Y. Zhang, O. Mosendz, U. Erugur, R. Yu, J. Tian, A. DeMann, S. B. Field, X. Yang, H. Ding, J. Tang, B. Terris, A. Fert, H. Chen, M. Wu, unpublished.

- [29] D. M. Pozar, *Microwave Engineering*, Wiley, Hoboken, NJ **2012**.
- [30] S. S. Kalarickal, P. Krivosik, J. Das, K. S. Kim, C. E. Patton, *Phys. Rev. B* **2008**, *77*, 054427.
- [31] S. S. Kalarickal, P. Krivosik, M. Wu, C. E. Patton, M. L. Schneider, P. Kabos, T. J. Silva, J. P. Nibarger, *J. Appl. Phys.* **2006**, *99*, 093909.
- [32] H. M. Olson, P. Krivosik, K. Srinivasan, C. E. Patton, *J. Appl. Phys.* **2007**, *102*, 023904.
- [33] J. M. Shaw, T. J. Silva, M. L. Schneider, R. D. McMichael, *Phys. Rev. B* **2009**, *79*, 184404.
- [34] H. L. Wang, C. H. Du, Y. Pu, R. Adur, P. C. Hammel, F. Y. Yang, *Phys. Rev. Lett.* **2014**, *112*, 197201.
- [35] L. A. Wray, S.-Y. Xu, Y. Xia, D. Hsieh, A. V. Fedorov, Y. S. Hor, R. J. Cava, A. Bansil, H. Lin, M. Z. Hasan, *Nat. Phys.* **2011**, *7*, 32.
- [36] J. Zhang, J. P. Velev, X. Dang, E. Y. Tsybal, *Phys. Rev. B* **2016**, *94*, 014435.
- [37] J. M. Marmolejo-Tejada, K. Dolui, P. Lazic, P.-H. Chang, S. Smidstrup, D. Stradi, K. Stokbro, B. K. Nikolic, *Nano Lett.* **2017**, *17*, 5626.
- [38] Y. T. Hsu, K. Park, E. A. Kim, *Phys. Rev. B* **2017**, *96*, 235433.
- [39] T. G. Pedersen, P. Modak, K. Pedersen, N. E. Christensen, M. M. Kjeldsen, A. N. Larsen, *J. Phys.: Condens. Matter* **2019**, *21*, 11.
- [40] B. Kardasza, O. Mosendz, B. Heinrich, Z. Liu, M. Freeman, *J. Appl. Phys.* **2008**, *103*, 07C509.
- [41] J. C. Rojas Sánchez, L. Vila, G. Desfonds, S. Gambarelli, J. P. Attané, J. M. De Teresa, C. Magén, A. Fert, *Nat. Commun.* **2013**, *4*, 2944.
- [42] Y. Xu, B. Yan, H.-J. Zhang, J. Wang, G. Xu, P. Tang, W. Duan, S.-C. Zhang, *Phys. Rev. Lett.* **2013**, *111*, 136804.
- [43] C.-Z. Xu, Y.-H. Chan, P. Chen, X. Wang, D. Flötotto, J. A. Hlevyack, G. Bian, S.-K. Mo, M.-Y. Chou, T.-C. Chiang, *Phys. Rev. B* **2018**, *97*, 035122.
- [44] G. J. de Coster, P. A. Folkles, P. J. Taylor, O. A. Vail, *Phys. Rev. B* **2018**, *98*, 115153.
- [45] V. A. Rogalev, F. Reis, F. Adler, M. Bauernfeind, J. Erhardt, A. Kowalewski, M. R. Scholz, L. Dudy, L. B. Duffy, T. Hesjedal, M. Hoesch, G. Bihlmayer, J. Schäfer, R. Claessen, *Phys. Rev. B* **2019**, *100*, 245144.
- [46] S.-Y. Xu, C. Liu, S. K. Kushwaha, R. Sankar, J. W. Krizan, I. Belopolski, M. Neupane, G. Bian, N. Alidoust, T.-R. Chang, H.-T. Jeng, C.-Y. Huang, W.-F. Tsai, H. Lin, P. P. Shibayev, F.-C. Chou, R. J. Cava, M. Z. Hasan, *Science* **2015**, *347*, 294.
- [47] M. Kargarian, M. Randeria, Y.-M. Lu, *Proc. Nat. Acad. Sci. USA* **2016**, *113*, 8648.